Basic Blocks for High-Frequency Interconnects: Theory and Experiment

HUNG-YU YANG AND NICÓLAOS G. ALEXOPOULOS, FELLOW, IEEE

Abstract — **Proximity-coupled open-end microstrip interconnects (transitions) in double-layer planar structures are investigated through the method of moments solution of integral equations. Two types of EMC (electromagnetically coupled) microstrip lines are considered, collinear lines and transverse lines. It is found that these interconnects are broad-band and provide wide range of coupling coefficient. The theoretical model for the transverse microstrip transition is in good agreement with measurements.**

I. INTRODUCTION

WITH the increasing complexity of microwave and millimeter-wave integrated circuits, passive component modeling becomes more and more important in accurately determining the performance of the designed circuits. However, up to now, most passive components are not well understood, especially junction discontinuities. Quasi-static analysis has been successfully applied to some discontinuities for low-frequency applications [1]. For higher frequencies, models based on rigorous dynamic analysis are required. The so-called spectral-domain approach [2] is one of these. Since an enclosed housing is assumed, radiation and surface wave effects are not considered in that approach. Recently, a more general approach, based on solving integral equations by the method of moments, has been applied to certain structures [3]–[6]. This method is applicable to shielded as well as open structures by using an appropriate Green's function. For open structures, this analysis may take into account all physical effects, including radiation, surface waves, and dominant as well as higher order mode coupling. Using this approach, two types of proximity-coupled open-end microstrip lines in a double-layer planar structure are investigated in this article. These proximity-coupled transitions constitute potentially important components for MIC and MMIC design. Fig. 1 shows two semi-infinite collinear microstrip lines at different levels. This type of transition has the advantage over the end-coupled lines in that the overlap distance l_{ol} may be used to control the coupling. Also this transition provides a wider range of coupling coefficients with a reasonably large bandwidth and it therefore may be used in coupler or filter design. Fig. 2 shows two EMC transverse microstrip lines. In this type of transition, an open-circuit microstrip line printed on top of the superstrate is crossed at a right angle by another open-circuit microstrip line embedded on the substrate. These two lines are extended a certain distance beyond the cross-junction to provide tuning stubs. This type of transition has the properties of broad-band and good match due to the presence of the double stub. The materials in the substrate–superstrate configuration may greatly affect the coupling in the transition, and this issue will also be investigated. In Section II, the method of moments solution of integral equations is formulated. Numerical techniques are developed to compute the double infinite integrations formulated in Section II, and this will be discussed in Section III. In Section IV, the results from the numerical analysis are presented and some interesting properties of the above-mentioned interconnects are discussed.

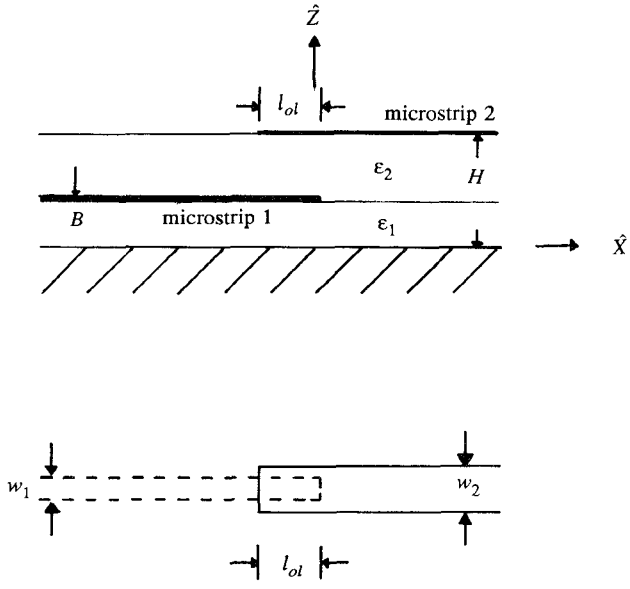

Fig. 1. Proximity-coupled collinear microstrip–microstrip transition.

Manuscript received January 27, 1988; revised March 14, 1988. This work was supported by the U.S. Army Research Office under Contract DAAG 03-83-k-0090 and by NSF Research Grant ECS-86-04837.

The authors are with the Electrical Engineering Department, University of California at Los Angeles, Los Angeles, CA 90024.

IEEE Log Number 8822041.

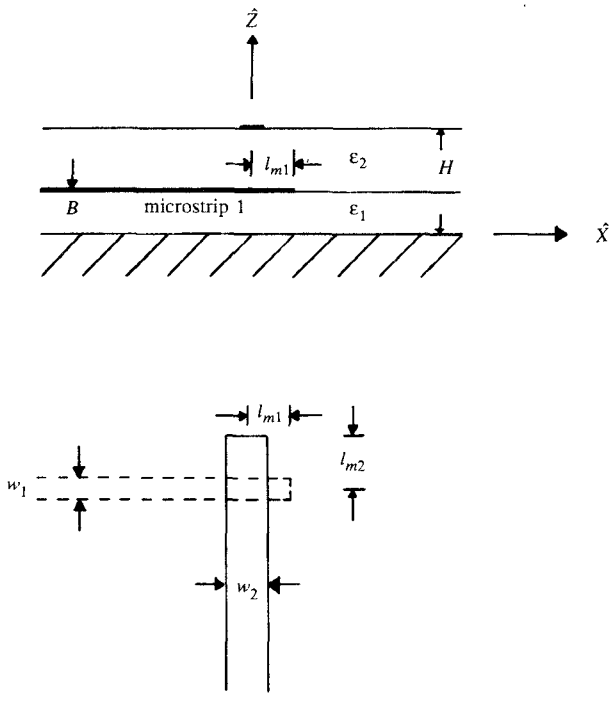

Fig. 2. Proximity-coupled transverse microstrip–microstrip transition.

II. Analysis

In practical circuit design, the width of the microstrip lines is much smaller than the effective wavelength; therefore, the transverse current in the microstrip is neglected for simplicity. Also, the transverse dependence of the longitudinal current is assumed such that the edge condition is enforced [3]–[6]. Under the above assumptions, integral equations can be formulated in terms of the longitudinal electric field on the microstrip.

A. EMC Collinear Microstrip Lines

Referring to Fig. 1, the integral equations for EMC collinear microstrip lines are

$$E_x^{(i)} = \sum_{j=1}^{2} \iint G_{ij} J_x^{(i)}\, ds_j \tag{1}$$

where $E_x^{(i)}$ is the electric field at microstrip i, $i=1$ or 2. Here microstrip 1 is at $z=B$ while microstrip 2 is at $z=H$. The Green's function G_{ij} is E_x at (x, y) of microstrip i due to an $\hat{x}$-directed delta source at (x_s, y_s) of microstrip j. This Green's function after solving the boundary value problem for the layered medium [7] can be expressed as

$$G_{ij} = \int_{-\infty}^{\infty}\int_{-\infty}^{\infty} D_{ij}(\lambda_x, \lambda_y) e^{-j\lambda_x(x-x_s)} e^{-j\lambda_y(y-y_s)}\, d\lambda_x\, d\lambda_y \tag{2}$$

where

$$D_{ij}(\lambda_x, \lambda_y) = \frac{-jZ_0}{4\pi^2 k_0 \epsilon_2}\left[\frac{k_2^2 - \lambda_x^2}{D_e(\lambda)} f_{ij}(\lambda) + \frac{\lambda_x^2 q_2}{D_e(\lambda) D_m(\lambda)} g_{ij}(\lambda)\right] \tag{3}$$

$$D_e(\lambda) = q_2\left(q + \frac{q_1}{\tanh q_1 B}\right)\cosh q_2(H-B) + q_2\left(q_2 + \frac{q_1 q}{q_2 \tanh q_1 B}\right)\sinh q_2(H-B) \tag{4}$$

$$D_m(\lambda) = q_2\epsilon_2(q\epsilon_1 + q_1 \tanh q_1 B)\cosh q_2(H-B) + \left(q_2^2\epsilon_1 + \epsilon_2^2 q_1 q \tanh q_1 B\right)\sinh q_2(H-B) \tag{5}$$

$$\lambda = \sqrt{\lambda_x^2 + \lambda_y^2} \tag{6}$$

$$q = \sqrt{\lambda^2 - k_0^2} \tag{7}$$

$$q_1 = \sqrt{\lambda^2 - k_1^2} \tag{8}$$

$$q_2 = \sqrt{\lambda^2 - k_2^2} \tag{9}$$

$$k_0 = \omega\sqrt{\mu_0\epsilon_0} \tag{10}$$

$$k_1 = k_0\sqrt{\epsilon_1} \tag{11}$$

$$k_2 = k_0\sqrt{\epsilon_2} \tag{12}$$

$$Z_0 = \sqrt{\mu_0/\epsilon_0}\,. \tag{13}$$

The functions $f_{ij}(\lambda)$ and $g_{ij}(\lambda)$ are defined in the Appendix.

In the method of moments procedure, the unknown currents $J_x^{(1)}$ and $J_x^{(2)}$ are expanded in terms of a set of known functions. An efficient and accurate scheme in mode expansion of the coupled semi-infinite lines is to use the basis functions that are composed of subdomain local modes and entire domain traveling wave modes [5], [6]. For example, the longitudinal dependence of the unknown current can be expanded as

$$f(x) = I^{\text{inc}} + I^{\text{ref}} + \sum_{n=1}^{N} I_{n1} f_n(x) \tag{14}$$

for the feed line (microstrip 1 here) and

$$g(x) = I^{t} + \sum_{n=1}^{M} I_{n2} g_n(x) \tag{15}$$

for the parasitic line (microstrip 2 here), where

$$I^{\text{inc}} = e^{-jk_{m1}x} \tag{16}$$

$$I^{\text{ref}} = -\Gamma e^{jk_{m1}x} \tag{17}$$

$$I^{t} = Te^{-jk_{m2}(x+l_{01})}. \tag{18}$$

Here k_{m1} and k_{m2} are the propagation constants of each microstrip line, which can be determined from a two-dimensional infinite line analysis [8]. Piecewise-sinusoidal (PWS) modes are used as subdomain modes and are defined from the end of each line [4]. These modes are

$$f_n(x) = \frac{\sin k_{e1}(d_1 - |x + nd_1|)}{\sin k_{e1} d_1} \qquad \text{for } |x + nd_1| < d_1 \tag{19}$$

and

$$g_n(x) = \frac{\sin k_{e2}(d_2 - |x + nd_1 + l_{ol}|)}{\sin k_{e2} d_2} \quad \text{for } |x + nd_2 + l_{ol}| < d_2 \quad (20)$$

where d_1 and d_2 are the half-length of the PWS mode in each line, respectively. The choice of k_{e1} and k_{e2} can be quite arbitrary. Here, they are chosen according to a treatise in numerical integration. This aspect will be discussed later. A nice feature of the combination of subdomain and entire domain modes is that when the method of moments is applied, the quantities of interest, Γ and T, are directly obtained by matrix inversion. Besides, the dimension of the impedance matrix is relatively small, typically < 20.

When the above expansion modes are used in (1), followed by Galerkin's procedure in the same way as described in [6], integral equations are converted into a set of linear equations. These $M + N + 2$ equations, when expressed in matrix form, are

$$\begin{bmatrix} [Z_{\text{self}_1}] & [Z_{t\,\text{self}_1}] & [Z_{ee\,\text{act}_2}] & [Z_{te\,\text{act}_2}] \\ [Z_{ee\,\text{act}_1}] & [Z_{te\,\text{act}_1}] & [Z_{\text{self}_2}] & [Z_{t\,\text{self}_2}] \end{bmatrix} \begin{bmatrix} [I_1] \\ -\Gamma \\ [I_2] \\ T \end{bmatrix} = \begin{bmatrix} [I_{\text{inc}_1}] \\ [I_{\text{inc}_2}] \end{bmatrix}. \quad (21)$$

The submatrices in (21) are the reaction of different basis functions. The matrix elements of $[Z_{\text{self}_i}]$ are the reaction of subdomain modes of the microstrip i, $i = 1$ or 2. The submatrix $[Z_{t\,\text{self}_i}]$ is the column matrix where its elements are the reaction between PWS modes and the entire domain reflected mode at microstrip i. The elements of submatrix $[Z_{ee\,\text{act}_1}]$ are the reaction between the PWS modes in the two different microstrip lines while the submatrix $[Z_{ee\,\text{act}_2}]$ is transpose to $[Z_{ee\,\text{act}_1}]$ due to reciprocity. The submatrix $[Z_{te\,\text{act}_i}]$ contains the elements which are the reaction between the entire domain reflected wave at microstrip i and the PWS mode at the other microstrip. The excitation submatrices $[I_{\text{inc}_1}]$ and $[I_{\text{inc}_2}]$ are much the same as the column matrices $[Z_{t\,\text{self}_1}]$ and $[Z_{te\,\text{act}_2}]$, respectively, except in the excitation matrix the entire domain incident wave instead of the reflected wave is used.

The computation of each matrix element in (21) requires double infinite integration where the integrand contains the corresponding Green's function $D_{tJ}(\lambda_x, \lambda_y)$ and the Fourier transform of the current expansion functions. Since the expression of these submatrices is in a form similar to that reported in [5] and [6], only $[Z_{\text{self}_1}]$ and $[Z_{ee\,\text{act}1_2}]$ are shown in the following to illustrate how the analysis is performed. $[Z_{\text{self}_1}]$ is an $(N+1)\times N$ matrix with matrix elements

$$Z^{nm}_{\text{self}_1} = \int_{-\infty}^{\infty}\int_{-\infty}^{\infty} D_{11}(\lambda_x, \lambda_y) F_1^2(\lambda_y) A_1^2(\lambda_x) \cdot \cos[\lambda_x (m-n) d_1]\, d\lambda_x\, d\lambda_y \quad (22)$$

and $[Z_{ee\,\text{act}_2}]$ is an $(N+1)\times M$ matrix with matrix elements

$$Z^{nm}_{ee\,\text{act}_2} = \int_{-\infty}^{\infty}\int_{-\infty}^{\infty} D_{12}(\lambda_x, \lambda_y) F_2(\lambda_y) \cdot F_1(\lambda_y) A_1(\lambda_x) A_2(\lambda_x) \cdot \cos[\lambda_x (nd_1 + md_2 - l_{ol})]\, d\lambda_x\, d\lambda_y \quad (23)$$

where

$$A_i(\lambda_x) = 2k_{ei} \frac{(\cos k_{ei} d_i - \cos \lambda_x d_i)}{(\lambda_x^2 - k_{ei}^2)} \quad (24)$$

$$F_i(\lambda_y) = J_0\left(\frac{w_i}{2}\lambda_y\right) \quad (25)$$

and $i = 1$ or 2. It can be observed from (23) and (24) that the integrand in the double infinite integration is composed of three factors multiplying one another. These are the Fourier-transformed Green's function, current expansion functions in Fourier domain, and the cosine function of the center distance between each expansion mode. This property is true for all the submatrices in (21). The method of numerical integrations of (22) and (23) will be discussed in Section IV.

B. EMC Transverse Microstrip Lines

The analysis of EMC transverse microstrip lines is almost one to one in correspondence to the collinear case. In matrix formulation, if local coordinates are used, it can easily be shown that the self-reaction in each microstrip is identical for the collinear and transverse cases. To be more specific, referring to Fig. 2, the integral equations for the transverse microstrip lines are

$$E_x^{(1)} = \iint G_{xx} J_x^{(1)} d_{s_1} + \iint G_{xy} J_y^{(2)} d_{s_2} \quad (26)$$

and

$$E_y^{(2)} = \iint G_{yx} J_x^{(1)} d_{s_1} + \iint G_{yy} J_y^{(2)} d_{s_2} \quad (27)$$

where $E_x^{(1)}$ and $E_y^{(2)}$ are the longitudinal electric fields at microstrip 1 (at $z = B$) and microstrip 2 (at $z = H$), respectively. The function G_{xx} is equal to G_{11}, while G_{yy} is the same as G_{22} except that λ_x and λ_y are interchanged in D_{22}. Other Green's functions are

$$G_{xy} = \int_{-\infty}^{\infty}\int_{-\infty}^{\infty} D_{xy}(\lambda_x, \lambda_y) e^{-j\lambda_x(x-x_s)} e^{-j\lambda_y(y-y_s)}\, d\lambda_x\, d\lambda_y \quad (28)$$

and

$$G_{yx} = G_{xy} \quad (29)$$

where

$$D_{xy}(\lambda_x, \lambda_y) = \frac{-jZ_0}{4\pi^2 k_0 \epsilon_2}\left[\frac{-\lambda_x\lambda_y}{D_e(\lambda)} f_{12}(\lambda) + \frac{\lambda_x\lambda_y q_2}{D_e(\lambda) D_m(\lambda)} g_{12}(\lambda)\right]. \quad (30)$$

The mode expansion mechanism and the method of moments procedure follow in the same manner as for the collinear case. The final matrix is in exactly the same form as (21). The submatrices $[Z_{\text{self}_i}], [Z_{t\,\text{self}_i}]$ with $i=1$ or 2 and $[I_{\text{inc}_1}]$ are identical for the collinear and transverse cases. All other submatrices can be obtained in a way similar to that for the longitudinal coupling case. For example,

$$Z^{nm}_{ee\,\text{act}_1} = -\int_{-\infty}^{\infty}\int_{-\infty}^{\infty} D_{xy}(\lambda_x,\lambda_y) F_2(\lambda_x) \cdot F_1(\lambda_y) A_1(\lambda_x) A_2(\lambda_y) \cdot \sin\left[\lambda_x(nd_1 - l_{m1})\right] \sin\left[\lambda_y(md_2 - l_{m2})\right] d\lambda_x\, d\lambda_y \tag{31}$$

where $[Z_{ee\,\text{act}_1}]$ is an $(M+1)\times N$ matrix. The parameters l_{m1} and l_{m2} are the stub lengths for microstrips 1 and 2, respectively. The sine function in (31) instead of a cosine in (24) is because the Green's function in (31) is an odd function of either λ_x or λ_y.

III. Numerical Integration

The double infinite integration in each matrix element is carried out numerically after transforming into polar coordinates. This procedure reduces the integration to a finite (0 to $\pi/2$) and an infinite (0 to ∞) integral. For the finite integral, a 32-point Gauss quadrature formula is used. For the infinite integral, special numerical methods are required. One can break the infinite integration range into two parts, $(0, A)$ and (A, ∞), such that in the first section the integrand contains singularities or derivative singularities, while for the second section the integrand is well behaved but slowly convergent. The choice of A is quite flexible, but it should satisfy $A > \max(k_1, k_2)$. The first integral contains surface wave poles whenever $D_e(\lambda)$ or $D_m(\lambda)$ becomes zero. If a pole extraction technique is applied [9], [10], in addition to the residue and Cauchy principal value, four sections of integrations are required due to the derivative singularities at $\lambda = k_0$, k_1, and k_2. The other way of performing the integration from 0 to A is to deform the contour off the real axis and apply the Cauchy Riemann theorem such that the integrand is well behaved [11]. This method is particularly useful in a multilayered structure, since it is not required to know the pole position, and the integration has no singularities. Both of the above-mentioned methods have been used and a negligible difference has been observed.

The second integration from A to ∞ is the so-called tail integration. This integration converges slowly when the testing and observation points are on the same plane (same z). Also, as λ gets larger, the integrand becomes a highly oscillating function. Although Filon's integration method can be applied, difficulty still exists, especially for small size basis function [8]. A more efficient and accurate method is to use an asymptotic extraction technique [12], [13]. This technique requires additional computations of the self and mutual reactions of PWS and entire domain modes in a homogeneous medium with dielectric constant ϵ_{eff}. It can be shown from the asymptotic behavior of the Green's function for a multilayered planar structure that this ϵ_{eff} is equal to the square root of the average of the dielectric constants right above and below the source point. Therefore, in this work we choose $k_{e1} = k_0\sqrt{(\epsilon_1+\epsilon_2)/2}$ and $k_{e2} = k_0\sqrt{(\epsilon_2+1)/2}$. With this technique, the convergence of the tail integration is improved by the order of λ^2. Also, by using entire domain basis functions, convergence can be improved. This is because the integrand will contain the Fourier transform of the entire domain mode, which decreases quickly away from the point where λ_x is equal to the phase constant (k_{m1} or k_{m2}).

IV. Results

Although the impedance matrix in (21) looks formidable, the computation can be further simplified based on some physical phenomena. For example, the Green's function and basis functions are the same in each submatrix except for a translation in reaction center. Therefore in the numerical process, these common factors need to be computed only once. Also, due to reciprocity, only part of the impedance elements need to be computed. The results have been compared for the special cases of an EMC collinear and an EMC transverse dipole fed by a microstrip line with results in [3] and [14], [15], respectively. Excellent agreement has been found for both theoretical and experimental results. In the present computations for the transition problem, entire domain modes three and a half guided wavelengths long and eight to 13 PWS modes (depending on the overlap or stub length) are used in each microstrip line. The convergence has been checked for $S_{11}(\Gamma)$, to within 3 percent in magnitude and 3° in phase. The magnitude of the reflection and transmission coefficients are shown in Figs. 3 and 4, respectively, as a function of overlap for the collinear transition with three types of material arrangements. The corresponding microstrip width is chosen such that the microstrip lines have 50 Ω characteristic impedance. For the case of large dielectric constant material in the substrate and a smaller one in the superstrate, since energy is mostly confined in the substrate, less power is transmitted than in other types of material arrangements. This behavior is observed in Figs. 3 and 4. From these two figures, one can see that the coupling coefficient depends on the amount of energy of an embedded microstrip stored in the superstrate. The relationship between overlap length and power distribution observed in Figs. 3 and 4 is not obvious. It can be explained empirically as follows. The amount of current induced in the parasitic line is mainly due to the longitudinal electric field generated by the open-end feed line. This current varies sinusoidally and decreases as the observation point moves farther away from the open end. Therefore, as the two microstrips are brought closer, increased coupling occurs. As the coupling gets stronger, the electric field due to the parasitic line will interact with the feed line

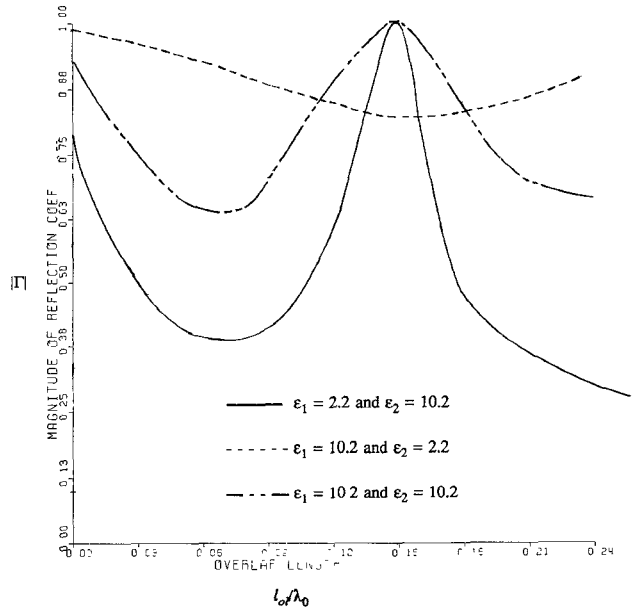

Fig. 3. $|\Gamma|$ versus overlap l_{ol} for an EMC 50 Ω–50 Ω collinear microstrip transition. $f = 10$ GHz, $H = 50$ mil, $B = 25$ mil.

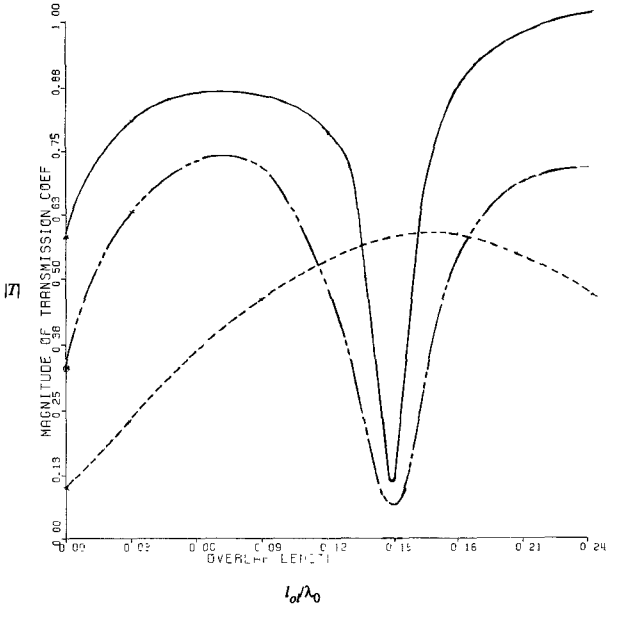

Fig. 4. $|T|$ versus overlap l_{ol} for an EMC collinear microstrip transition. Parameters are the same as those in Fig. 3.

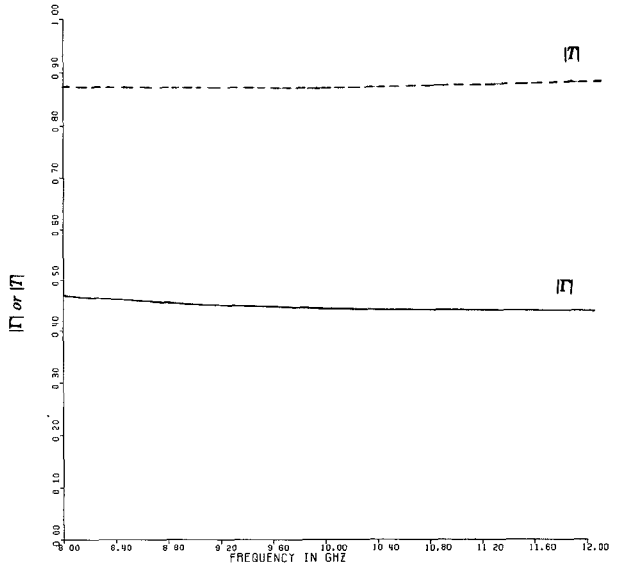

Fig. 5. $|\Gamma|$ and $|T|$ versus frequency. $l_{ol} = 0.15$ cm, $\epsilon_1 = 2.2$, and $\epsilon_2 = 10.2$. $H = 50$ mil, $B = 25$ mil, $w_1 = 42$ mil, and $w_2 = 76$ mil.

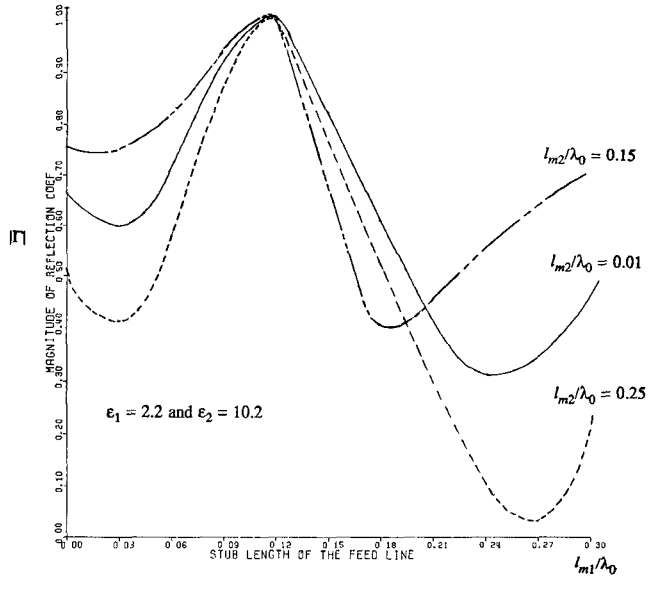

Fig. 6. $|\Gamma|$ as a function of stub length for a 50 Ω–50 Ω transverse transition. $f = 10$ GHz, $H = 50$ mil, $B = 25$ mil, $w_1 = 42$ mil, and $w_2 = 76$ mil.

field. Since these two microstrip lines guide different modes, as the overlap increases further, the coupling starts to decrease due to wave destructive interference. It is interesting to see that with a particular overlap length, very little coupling occurs. This behavior is found to be related to the superstrate thickness and dielectric constant. It is also observed that as the overlap gets larger, the reflection becomes smaller. This implies that in such a case, the guided fundamental mode is more like the coupled line mode. It is further found from Figs. 3 and 4 that in a certain region where coupling reaches a local maximum, the scattering matrix is insensitive to overlap length. Since the line impedance and effective dielectric constant are also frequency insensitive, in this microstrip transition, only the effective overlap length will be frequency sensitive. This implies that this transition is broad-band. An example is shown in Fig. 5. One can see that the scattering parameters change no more than 3 percent in magnitude for this particular X-band computation.

For the transverse microstrip transition, the material also has a strong effect on the coupling mechanism, as shown in Figs. 6 and 7. The coupling between two transverse microstrips is further complicated by the presence of two tuning stubs. The effect of these two stubs is very much different from those in the microstrip–slotline transition [1] and [6], where optimum coupling occurs when both stubs are about a quarter wavelength long. For the transverse microstrip transition, the coupling is minimum

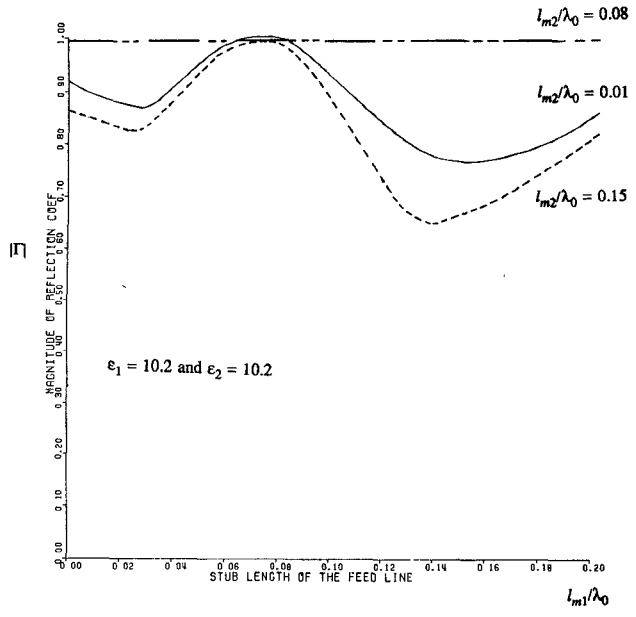

Fig. 7. $|T|$ as a function of stub length for a 50Ω–50 Ω transverse transition. $f = 10$ GHz, $H = 50$ mil, $B = 25$ mil, $w_1 = 16$ mil, and $w_2 = 50$ mil.

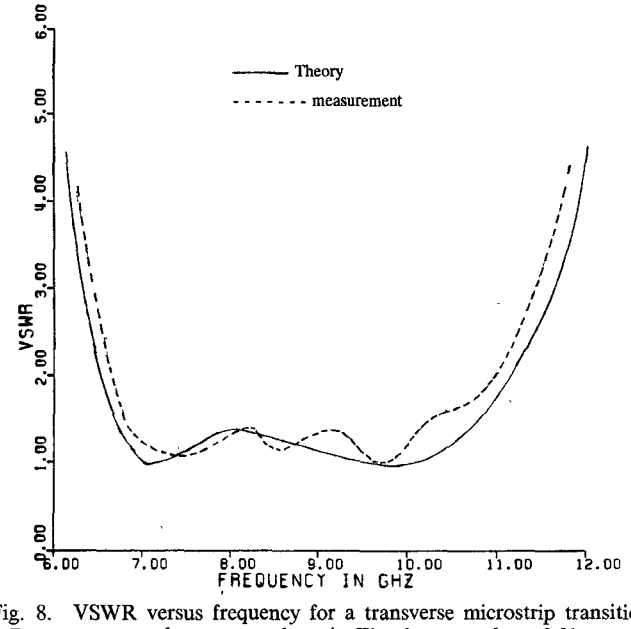

Fig. 8. VSWR versus frequency for a transverse microstrip transition. Parameters are the same as those in Fig. 6, except $l_{m1} = 0.81$ cm and $l_{m2} = 0.75$ cm. ——— theory; ---- measurement.

when either stub is about a quarter wavelength and is maximum when both stubs are half a wavelength long. This phenomenon is due to the fact that the parasitic line, from a circuit point of view, is a shunt element to the feed line, and vice versa. Therefore, when both stubs are half a wavelength long, the circuit, looking from the cross junction, is in resonance, while when either stub is about a quarter wavelength long, the circuit is in effect shorted. For the parameters in Fig. 6, the guided wavelength for each microstrip is approximated as $\lambda_{m1} = 0.547\lambda_0$ and $\lambda_{m2} = 0.507\lambda_0$, while in Fig. 7 the guided wavelength is $\lambda_{m1} = 0.321\lambda_0$ for microstrip 1 and $\lambda_{m2} = 0.360\lambda_0$ for microstrip 2. In Fig. 6, maximum coupling occurs when both stubs l_{m1} and l_{m2} are about half a guided wavelength. In this particular case, one can see that the VSWR of this transition can be as small as 1.1. Therefore, this transition can be potentially useful in two-level circuit design.

To verify the performed analysis, a 3 inch by 2 inch circuit has been built and tested for the case of transverse microstrip transition. Duroid materials with permittivity 2.2 and 10.2 are used as the substrate and the superstrate, respectively. The dimensions of the device are chosen to be the same as those in Fig. 6 except that stub lengths of about half a guided wavelength are used (0.75 cm and 0.81 cm for the top and bottom microstrip, respectively). The circuit is made by a standard photoetching technique and measured by the HP-8510 network analyzer. Both computed and measured results for VSWR are shown in Fig. 8. The comparison shows good agreement. The ripple observed in the measurement may be due to the imperfect match at the coaxial–microstrip transitions. One can observe that the VSWR is less than 1.8 from 7 to 11 GHz. Such a broad-band transition would be very useful in circuit design. This broad-band property is mainly attributed to the double resonance due to the presence of double stubs. In this investigation, 50 Ω microstrip lines are used. The impedance level will affect coupling in the transition. Therefore, the results presented here may not be optimized. The choice of the impedance level may depend upon the purpose of the circuit design.

V. Conclusion

Two types of proximity-coupled open-end microstrip transitions are investigated theoretically; these are the EMC collinear and transverse transitions. The results obtained from the method of moments solution of integral equations are compared with measurement, with good agreement. It is found that the collinear transition can be potentially used in microwave coupler or filter design due to its properties of large bandwidth and wide range of coupling coefficient. The transverse transition is particularly useful for two-level circuit design where the VSWR can be nearly 1 over a wide range of frequency.

Appendix

Certain functions defined in Section II are explicitly described in this Appendix. Functions $f_{ij}(\lambda)$ and $g_{ij}(\lambda)$ in (3) are expressed as

$$f_{11}(\lambda) = q\sinh q_2(H-B) + q_2\cosh q_2(H-B) \tag{A1}$$

$$g_{11}(\lambda) = (\epsilon_1-\epsilon_2)f_{11}(\lambda)[q\epsilon_2\cosh q_2(H-B) + q_2\sinh q_2(H-B)] + \epsilon_2(1-\epsilon_2)q_1q_2\tanh q_1B \tag{A2}$$

$$f_{22}(\lambda) = \frac{q_1\sinh q_2(H-B)}{\tanh q_1B} + q_2\cosh q_2(H-B) \tag{A3}$$

$$g_{22}(\lambda) = (1-\epsilon_2)\left[q_1\epsilon_2 \cosh q_2(H-B)\tanh q_1 B + q_2\epsilon_1 \sinh q_2(H-B)\right] \cdot f_{22}(\lambda) + \epsilon_2(\epsilon_1-\epsilon_2)qq_2 \quad \text{(A4)}$$

$$f_{12}(\lambda) = q_2 \quad \text{(A5)}$$

$$g_{12}(\lambda) = \epsilon_2(1-\epsilon_2)f_{22}(\lambda)q_1 \tanh q_1 B + (\epsilon_1-\epsilon_2)q_2\left[q\epsilon_2 \cosh q_2(H-B) + q_2 \sinh q_2(H-B)\right] \quad \text{(A6)}$$

$$f_{21}(\lambda) = f_{12}(\lambda) \quad \text{(A7)}$$

and

$$g_{21}(\lambda) = g_{12}(\lambda). \quad \text{(A8)}$$

ACKNOWLEDGMENT

The authors would like to thank O. Fordham at Hughes Aircraft Company for his help with the experimental part of this research.

REFERENCES

[1] K. C. Gupta, R. Gary and I. J. Bahl, *Microstrip Lines and Slotlines*. Dedham, MA: Artech House, 1979.

[2] R. H. Jansen, "The spectral domain analysis for microwave integrated circuits," *IEEE Trans. Microwave Theory Tech.*, vol. MTT-33, pp. 1043–1056, Oct. 1985.

[3] P. B. Katehi and N. G. Alexopoulos, "On the modeling of electromagnetically coupled microstrip antennas—The printed dipole," *IEEE Trans. Antennas Propagat.*, vol. AP-32, pp. 1179–1186, Nov. 1984.

[4] P. B. Katehi and N. G. Alexopoulos, "Frequency-dependent characteristics of microstrip discontinuities in millimeter wave integrated circuits," *IEEE Trans. Microwave Theory Tech.*, vol. MTT-33, pp. 1029–1035, Oct. 1985.

[5] R. W. Jackson and D. M. Pozar, "Fullwave analysis of microstrip open-end and gap discontinuities," *IEEE Trans. Microwave Theory Tech.*, vol. MTT-33, pp. 1036–1042, Oct. 1985.

[6] H. Y. Yang and N. G. Alexopoulos, "A dynamic model for microstrip-slotline transition and related structures," *IEEE Trans. Microwave Theory Tech.*, vol. 36, pp. 286–293, Feb. 1988.

[7] N. G. Alexopoulos and D. R. Jackson, "Fundamental superstrate (cover) effects on printed circuit antennas," *IEEE Trans. Antennas Propagat.*, vol. AP-32, pp. 807–815, Aug. 1984.

[8] D. R. Jackson and N. G. Alexopoulos, "Analysis of planar strip geometries in a substrate-superstrate configuration," *IEEE Trans. Antennas Propagat.*, vol. AP-34, pp. 1430–1438, Dec. 1986.

[9] I. E. Rana and N. G. Alexopoulos, "Current distribution and input impedance of printed dipoles," *IEEE Trans. Antennas Propagat.*, vol. AP-29, pp. 99–106, Jan. 1981.

[10] I. E. Rana and N. G. Alexopoulos, "Correction to 'Current distribution and input impedance of printed dipoles' and 'Mutual impedance computation between printed dipoles'," *IEEE Trans. Antennas Propagat.*, vol. AP-30, p. 822, July 1982.

[11] E. H. Newman and D. Forrai, "Scattering from a microstrip patch," *IEEE Trans. Antennas Propagat.*, vol. AP-35, pp. 245–251, Mar. 1987.

[12] J. Mosig and F. Gardiol, "A dynamic radiation model for microstrip structures," *Advances in Electronics and Electron Physics*, vol. 59, pp. 139–237, 1982.

[13] D. M. Pozar, "Improved computational efficiency for the method of moments solution of printed dipoles and patch," *Electromagnetics*, vol. 3, nos. 3–4, pp. 299–309, Jul.–Dec. 1983.

[14] P. Lepeltier, J. M. Floc'h and J. Citerne, "Complete and rigorous analysis of the electromagnetically coupled transverse microstrip dipole," *Electron. Lett.*, to be published.

[15] P. Lepeltier, J. M. Floc'h, J. Citerne and D. Martin, "On the excitation microstrip line parasitic radiation observed in printed antennas—The EMC dipole," in *Proc. IEEE Antenna Propagat. Soc. Int. Symp.* (Blacksburg), June 1987, pp. 814–818.

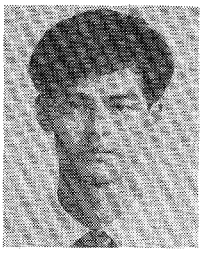

Hung-Yu Yang was born in Taipei, Taiwan, on October 25, 1960. He received the B.S. degree in electrical engineering from National Taiwan University in 1982 and the M.S. degree in electrical engineering from the University of California at Los Angeles in 1985.

During the years 1982–1984 he served in the R.O.C. Navy as an electronics officer. He is currently pursuing the Ph.D. degree at the University of California at Los Angeles. His research interests are in printed-circuit antennas and the modeling of microwave and millimeter-wave devices.

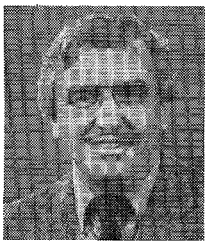

Nicólaos G. Alexopoulos (S'68–M'69–SM'82–F'87) graduated from the 8th Gymnasium of Athens, Greece, and subsequently obtained the B.S.E.E., M.S.E.E., and Ph.D. degrees from the University of Michigan, Ann Arbor, in 1964, 1967, and 1968, respectively.

Currently he is Professor and Chairman of the Electrical Engineering Department at the University of California, Los Angeles. He is also a Consultant with Northrop Corporation's Advanced Systems Division. Dr. Alexopoulos is the Associate Editor of the *Electromagnetics Journal* and *Alta Frequenza* and is on the Editorial Boards of the IEEE TRANSACTIONS ON MICROWAVE THEORY AND TECHNIQUES and the *International Journal on Electromagnetics Theory*. He served as the 1974 Chairman of the IEEE AP-S Chapter. He is the corecipient of the 1983 IEEE AP-S R. W. P. King Best Paper Award and of the 1984 IEEE Antennas and Propagation Society's Schelkunoff Prize (Best Paper Award).

His current research interests are in electromagnetic theory as it applies to the modeling of integrated-circuit components and printed circuit antennas for microwave and millimeter-wave applications, substrate materials and their effect on integrated-circuit structures and printed antennas, integrated-circuit antenna arrays, and antenna scattering studies. He is furthermore interested in the interaction of electromagnetic waves with materials and, in particular, active media.